Investigation of light absorption properties and acceptance angles of nanopatterned GZO/a-Si/p $^{+}$ -Si photodiodes

2010 Nanotechnology 21 215201

(http://iopscience.iop.org/0957-4484/21/21/215201)

Nanotechnology **21** (2010) 215201 (7pp) doi:10.1088/0957-4484/21/21/215201

Investigation of light absorption properties and acceptance angles of nanopatterned GZO/a-Si/p^+-Si photodiodes

Cheng-Pin Chen[1], Pei-Hsuan Lin[1], Yen-Jen Hung[1], Shao-Shun Hsu[1], Liang-Yi Chen[1], Yun-Wei Cheng[1], Min-Yung Ke[1], Ying-Yuan Huang[1], Chun-Hsiang Chang[1], Ching-Hua Chiu[2], Hao-Chung Kuo[2] and JianJang Huang[1,3,4]

[1] Graduate Institute of Photonics and Optoelectronics, National Taiwan University, Taipei 106, Taiwan
[2] Department of Photonics and Institute of Electro-Optical Engineering, National Chiao-Tung University, Hsinchu 300, Taiwan
[3] Department of Electrical Engineering, National Taiwan University, Taipei 106, Taiwan

E-mail: jjhuang@cc.ee.ntu.edu.tw

Received 1 January 2010, in final form 7 April 2010
Published 30 April 2010
Online at stacks.iop.org/Nano/21/215201

Abstract
In this work, n-GZO/a:amorphous-Si(i:intrinsic)/p^+-Si photodiodes are fabricated. We employed a nanosphere lithographic technique to obtain nanoscale patterns on either the a-Si(i) or p^+-Si surface. As compared with the planar n-GZO/p^+-Si diode, the devices with nanopatterned a-Si(i) and nanopatterned p^+-Si substrates show a 32% and 36.2% enhancement of photoresponsivity. Furthermore, the acceptance angle measurement reveals that the nanostructured photodiodes have larger acceptance angles than the planar structure. It also shows that the device with the nanocone structure has a higher acceptance angle than that with the nanorod structure.

(Some figures in this article are in colour only in the electronic version)

1. Introduction

The efficiency of solar cells can be improved by several key factors such as the employment of light trapping structures, the utilization of the full solar spectrum, and the technique of achieving wide acceptance angles. In the past, periodic textured surfaces [1–3], transparent conductive oxide (TCO) coatings [4–6], nanowires [7–9], random rough surfaces and the design of surface plasmons [10–12] have been reported to reduce the surface reflectivity of the device so that more photons can be trapped. Furthermore, multi-junction and tandem structures have been proposed to fully utilize the solar energy by efficiently absorbing the solar spectrum or recycling the reflected incident light for absorption [13–15]. We previously proposed a photodiode with n-ZnO/p-Si structure that possesses a wide absorption spectrum from the near ultraviolet to near infrared range [16]. Moreover, by spin-coating a monolayer of silica nanoparticles on the sample surface, the acceptance can be greatly improved.

Most reported technologies to improve light trapping in solar devices are targeting texturing (or coating TCO on) the light incident surface. There have also been reports in which the intrinsic light absorption layers were grown above the texturing surface [5, 6]. And some presented the subject of sub-wavelength morphology in the intrinsic light absorption layer [17, 18]. The nanoscale patterns in the intrinsic light absorbing layer have several advantages. In addition to a more efficient light interaction with the textured layer, the sub-wavelength periodicity has a similar size to the intrinsic layer thickness, which reduces the transit time for generated carriers to travel to the contact electrodes.

In this work, we fabricated n-GZO(ZnO doped with Ga)/a(amorphous)-Si(i)(i:intrinsic)/p^+-Si photodiodes. By employing a nanosphere lithographic technology, either the

[4] Author to whom any correspondence should be addressed.

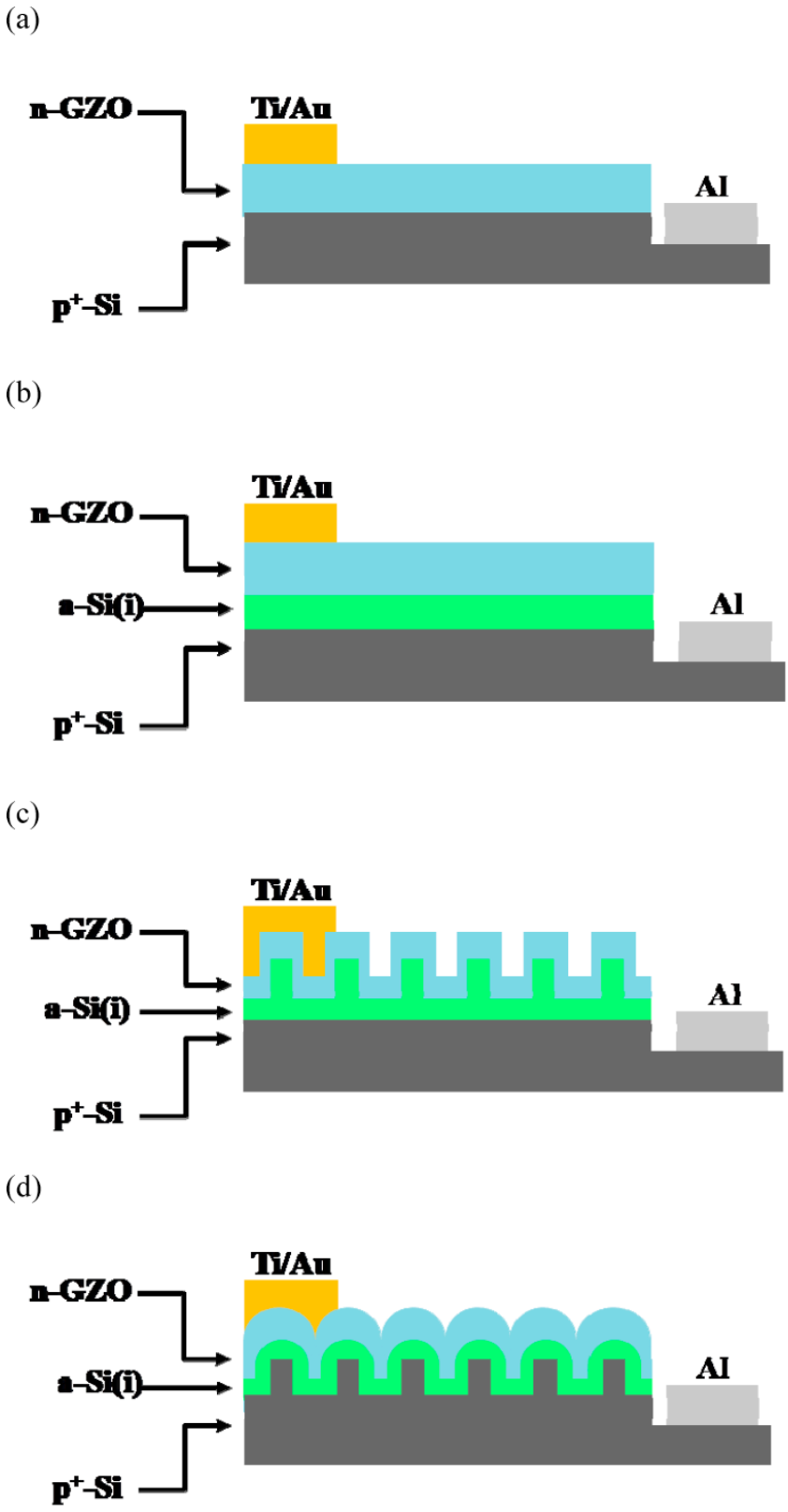

Figure 1. Device structures of (a) planar GZO/p^+-Si (device A), (b) planar GZO/a-Si(i)/p^+-Si (device B), (c) GZO/nanopatterned a-Si(i)/p^+-Si (device C) and (d) GZO/a-Si(i)/nanopatterned p^+-Si (device D).

a-Si(i) or p^+-Si was textured with a period in the range around 100–200 nm. We compared the photoresponsivity of four samples with and without the a-Si(i) layer and surface texturing. In order to understand the effect of sub-wavelength texturing on the acceptance angle, light absorption measurements at different incident angles were also conducted.

2. Device fabrication

The n-GZO/p^+-Si photodiodes were mainly realized by stacking n-type GZO on top of the p^+-type Si substrate. To investigate the effect of texturing on light absorption either the intrinsic a-Si or the p^+-Si substrate was patterned in the nanoscale. The device structures in this work are sketched in figure 1. Devices A, B, C and D represent the planar n-GZO/p^+-Si, planar n-GZO/a-Si(i)/p^+-Si, n-GZO/nanopatterned a-Si(i)/p^+-Si and n-GZO/a-Si(i)/nanopatterned p^+-Si structures, respectively. Prior to the device fabrication, the p^+-Si substrates were treated in RCA and diluted HF to remove organic and oxide residuals. For devices B, C and D, the 200 nm-thick a-Si(i) layers were deposited on the p^+-Si by HDP-CVD (high density plasma-chemical vapor deposition; Duratek system, Multiplex Cluster CVD). And the n-GZO layers for all four samples were deposited by RF magnetron sputtering using a ZnO target doped with 3 wt% Ga. The n-GZO layer is 200 nm in thickness with a doping density 2×10^{20} cm^{-3} after annealing at 400 °C for 30 min. For devices C and D, the nanopatterns were realized by using nanosphere lithography. We first spin-coated a monolayer of silica nanoparticles, which are resolved in the IPA (isopropyl alcohol) solvent, on the sample, followed by RIE (reactive ion etching) to define the nanopatterns. The silica nanoparticles with a diameter 100 nm $\pm$ 10 nm act as a hard mask during the pattern definition. And the etch depth is around 70 nm. The corresponding SEM (scanning electron microscopic) images of the nanopatterns on the p^+-Si and the a-Si(i) thin film on the nanopatterned p^+-Si substrate are demonstrated in figures 2(a) and (b), respectively. The spacing between the nanostructures, calculated from the top view of a SEM photo, is around 100–200 nm, with an average of 144.55 nm by assuming a triangular arrangement of nanoparticles. Figure 2(a) shows the surface morphology of the nanopatterned p^+-Si substrate after the RIE process with a 70 nm etching depth. Furthermore, figure 2(b) shows the surface profile with a 200 nm-thick a-Si(i) thin film deposited on the nanopatterned p^+-Si substrate. Basically, the SEM image of the a-Si/nanopatterned p^+-Si sample reveals a smoother nanorod profile than that of the nanopatterned p^+-Si. Below, we define the smoother nanopatterns of device D as a nanocone while the surface of device C as a nanorod profile (see figure 1 for illustration). Finally, Al (200 nm) and Ti/Au (12 nm/200 nm) were evaporated as the p-type and n-type contact electrodes, respectively. They were separately alloyed to achieve optimum contact conditions. For all the samples investigated, the mesa area is 300×300 μm^2.

3. Characterizations of photodiodes

3.1. Electrical properties

The electrical properties were characterized using an Agilent 4155C semiconductor parameter analyzer. As shown in the inset of figure 3, the I–V curves are linear for both Ti/Au contacts on the planar n-GZO (right) and Al on the planar p^+-Si (left), respectively, indicating the formation of ohmic contacts on the n- and p-pads. And from figure 3, the dark current–voltage (I–V) curves suggest a nonlinear rectifying behavior for all devices. The leakage currents are 99.2 nA, 67.6 nA, 355.2 nA and 108.3 nA for devices A, B, C and D, respectively, at a bias voltage of -2.5 V. From the figure we can also observe an increase in forward voltage for devices B, C and D, which is attributed to the insertion of the intrinsic a-Si thin layer.

(a)

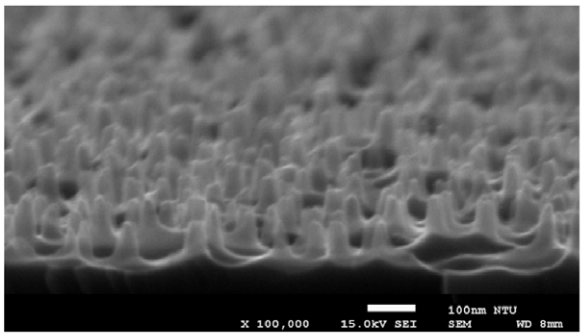

(b)

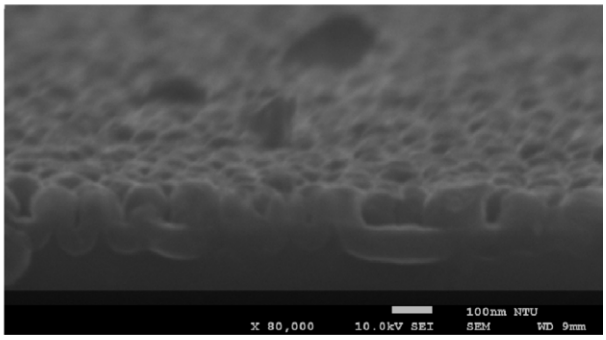

Figure 2. SEM photos of a nanopatterned p^+-Si substrate (a) and of a 200 nm-thick a-Si thin film on nanopatterned p^+-Si substrate (b).

3.2. Optical properties

The optical response was measured by illuminating the samples with monochromatic light from a xenon lamp (SP CM110 1/8 Monochromator) on the GZO side. As demonstrated in figure 4, the photoresponsivity of device A is basically composed of near band edge absorption of p^+-Si at the wavelength range between 600 and 800 nm, along with near the n-GZO band edge and n-GZO/p^+-Si heterojunction absorption at the wavelength around 350–600 nm. The average photoresponsivity at the wavelength between 350 and 800 nm is 0.13 A W^{-1} for device A. As for device B, a peak wavelength at 530 nm with an average photoresponsivity 0.08 A W^{-1} was demonstrated. The main peak at the green band is attributed to the dominant absorption in the intrinsic a-Si layer. Also, the decrease of photoresponsivity for device B, as compared with device A, can be ascribed to the potential increase of defects at both a-Si(i)/p^+-Si and n-GZO/a-Si(i) heterojunctions as both a-Si(i) and n-GZO layers were grown in different chambers. In contrast, device A possesses only one heterojunction (only one interface for defects). In addition, the 200 nm-thick a-Si(i) in device B is likely to block optical

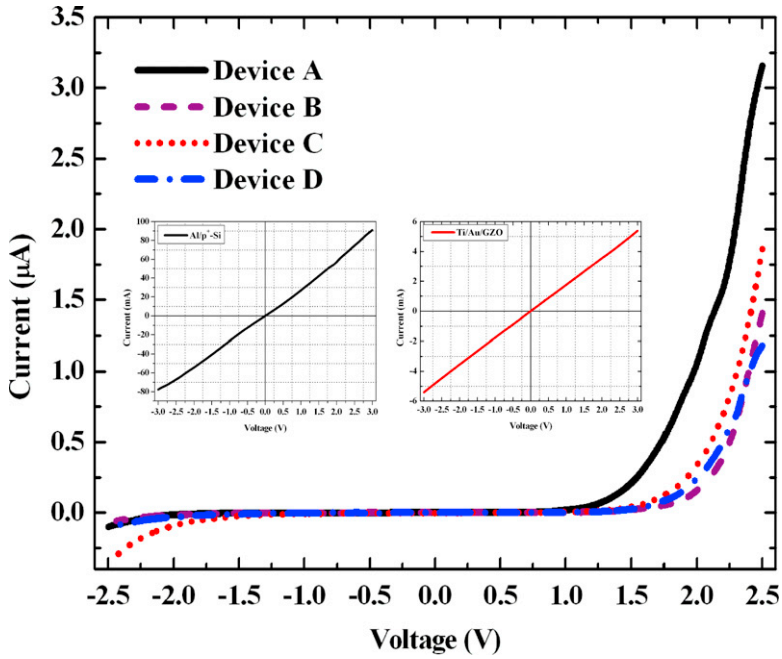

Figure 3. I–V curves of the photodiodes under comparison (insets: (left) the I–V curve of the Al contact on p^+-Si; (right) the I–V curve of the Au/Ti contact on n-ZnO. Both curves show good ohmic contact).

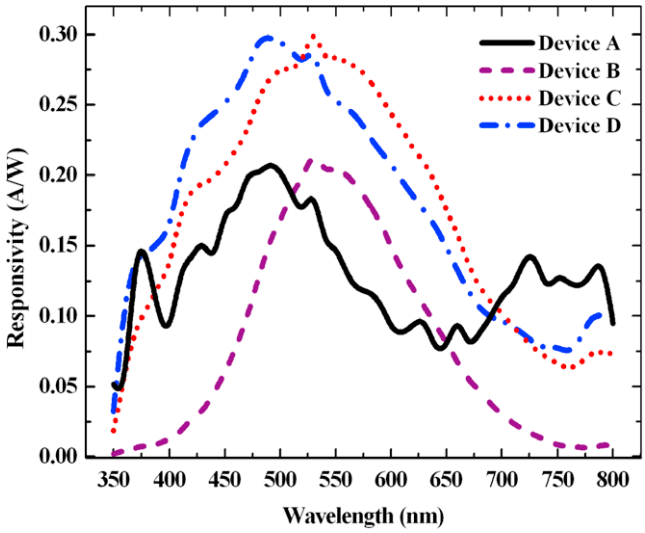

Figure 4. Photoresponsivity curves of devices A, B, C, and D.

transmission to p^+-Si, resulting in a lower photoresponsivity in the wavelength range 600–800 nm. On the other hand, devices C and D show 32% and 36.2% enhancement of photoresponsivity over that of device A. Also, the responsivity curves of devices C and D possess peaks near the green wavelength range. It implies that despite the existence of two heterojunctions (two interfaces of potential pick-up of defects), the responsivity of the structure with nanopatterned a-Si or p^+-Si is much higher than that of the planar device.

To understand the effect of nanopatterns on the photocurrents, the optical reflectivity was extracted on several material surfaces. The optical reflections were measured from nearly normal light incidence (5° offset) covering the wavelength between 300 and 800 nm with a standard UV–vis (ultraviolet–visible) spectrometer (JASCO ARN-733) and an integrating sphere and the noise level is around 0.002%. As shown in figure 5(a), the reflectivity of the nanopatterned p^+-Si surface is significantly reduced as compared to that of the flat p^+-Si surface. We also observe an even more significant decrease of reflectivity at the shorter wavelength. At the wavelength 443 nm, the reflectivity of the nanopatterned p^+-Si is 26.21% smaller than that of the flat p^+-Si surface, as compared to 7.86% smaller at 800 nm, which is attributed to a more effective interaction between the nanostructure and the incident light at short wavelength as both sizes are comparable due to the grating effect. In addition, the reflectivity comparison between planar a-Si(i) and nanopatterned a-Si(i) on the planar p^+-Si substrate also demonstrates a similar trend. However, both the reflectivity of the planar surface and the percentage decrease between flat and nanostructured a-Si(i) are smaller than the case in figure 5(a). Since the a-Si(i) layer is grown by HDP-CVD, the surface morphology on the 'flat' a-Si(i) surface is already rougher than that on the flat p^+-Si substrate. Therefore, the percentage reduction of reflectivity in figure 5(b) at the short wavelength is not as significant as that in figure 5(a).

The observation of the lower reflectivity at the shorter wavelength indicates the responsivity peaks of devices C and D, in figure 4, are blue shifted from that of device B. And the further blue shift that device D exhibits is attributed to a lower reflectivity in the nanopatterned p^+-Si surface at the shorter wavelength (around 443 nm), by comparing the optical properties with device C. Another explanation of the further blue shift of device D is related to the photocurrents induced at the short wavelength. As pointed out above, the responsivity at the 300–600 nm wavelength range is mainly contributed

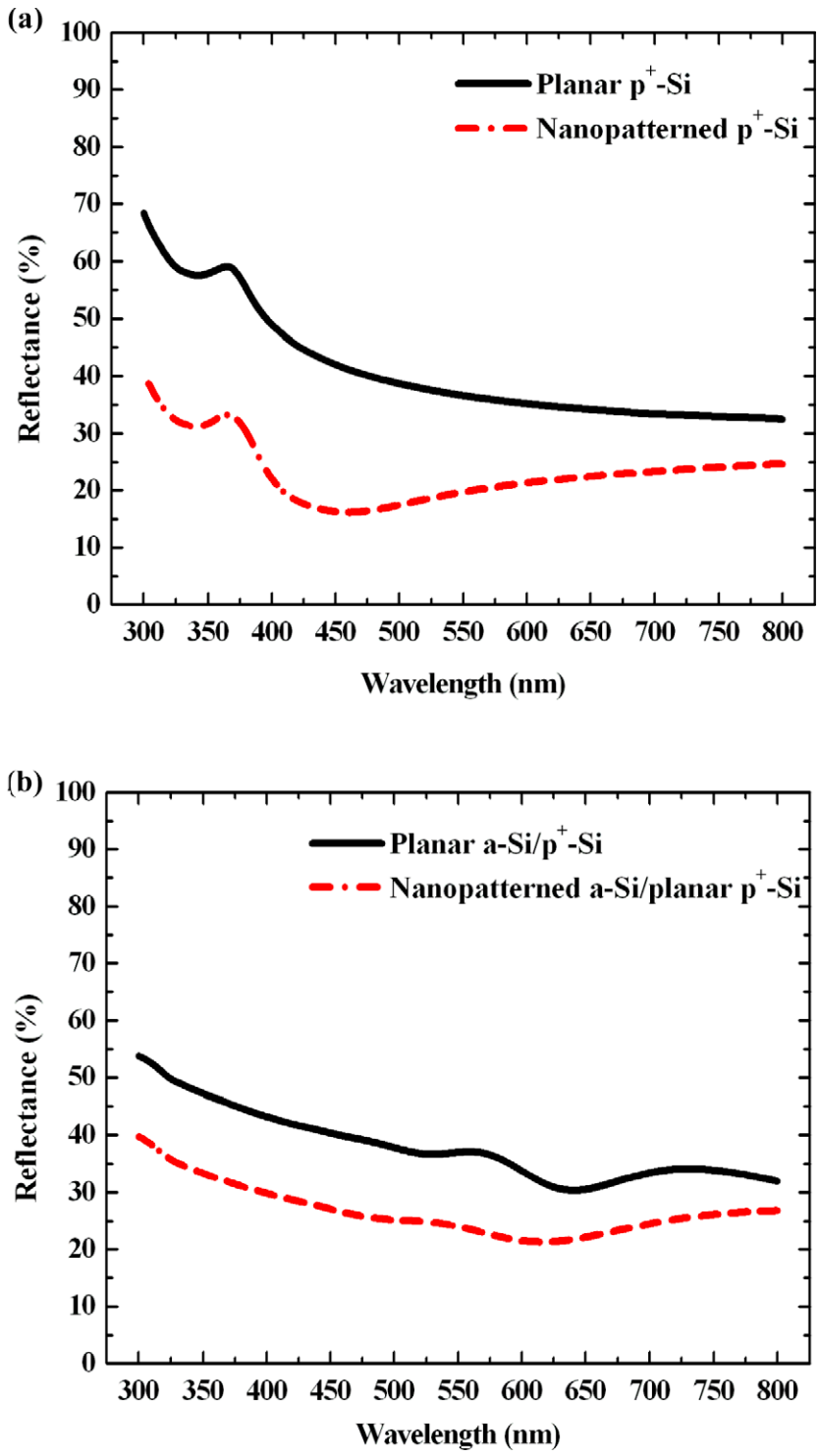

Figure 5. Comparisons of the reflectivity between planar and nanopatterned p^+-Si surfaces (a), and planar a-Si and nanopatterned a-Si layers on planar p^+-Si substrates (b).

by the absorption in the n-GZO layer and the n-GZO/a-Si(i) heterojunction. Since the nanopatterns on device C are realized by the dry etching on a-Si(i), the n-GZO/a-Si(i) interface suffers from etching damage and more defects are picked up in the interface. Therefore, the photocurrent at the blue–UV wavelength range of device C is lower than that of device D. Likewise, the etching damage on p^+-Si of device D results in more defects in the a-Si(i)/p^+-Si junction and less photocurrents in accordance. Moreover, in addition to the photon transmission and absorption processes in the semiconductor layers, the photoresponsivity is also related to the generated carrier transit time across the p–i–n diodes to complete the current conducting path. Since the nanopatterned a-Si has a thinner effective thickness, carriers generated in the ZnO and p^+-Si can quickly escape to the contact electrodes.

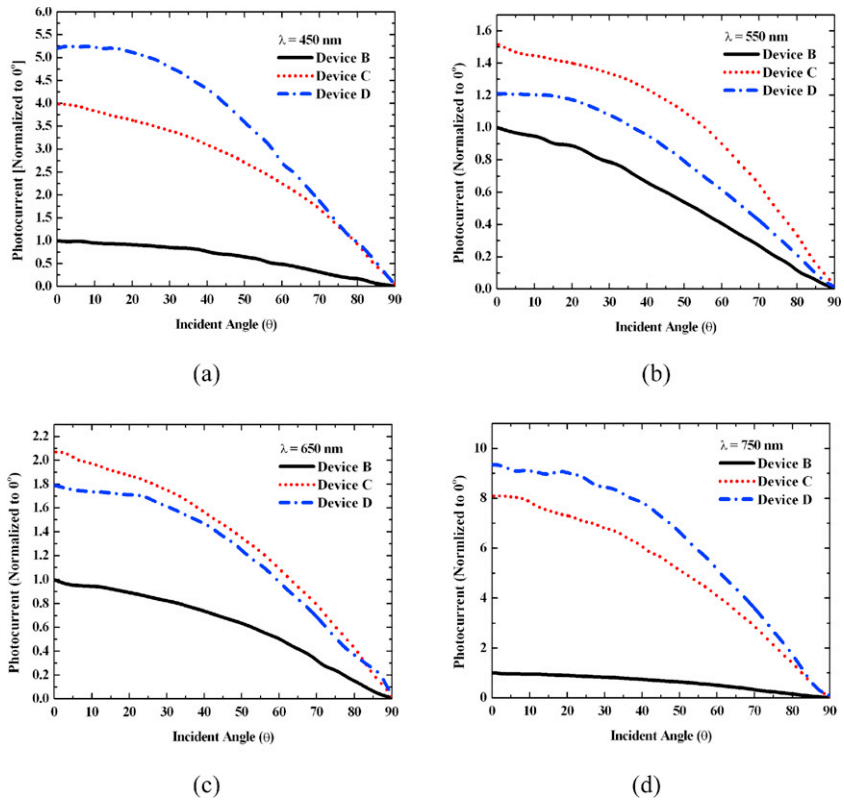

Figure 6. Comparisons of the acceptance angles of devices B, C, and D at the wavelength 450 nm (a), 550 nm (b), 650 nm (c) and 750 nm (d). The photocurrents are normalized to that of the conventional photodiode at 0°.

We next investigate the effect of the nanopatterned surface on the acceptance angle of the photodiodes with the a-Si(i) layer, i.e. devices B, C and D. The angle dependent photoresponsivity measurement was performed by illuminating the samples with a uniform and constant optical density of light source at various wavelengths using the setup described in the previous research [16]. In this experiment, the samples were illuminated at a distance 50 mm away from the light source. For ease of comparison, at different wavelengths, photocurrents of devices C and D are normalized to that of device B in the vertical direction (0°). In figure 6, the normalized photocurrents of devices B, C and D are plotted under different incident angles at the major visible wavelengths 450, 550, 650, and 750 nm. Basically, for device B, the photocurrent decays continuously as the incident angle is tilted since the effective radiative energy received by the device becomes smaller. The acceptance angle of device B, defined as the incident angle at 90% of the maximum light absorption, is 20°, 17°, 18° and 18° at the wavelength 450 nm, 550 nm, 650 nm and 750 nm, respectively. In comparison, the acceptance angles of devices C and D demonstrate an increase. They become 22°, 25°, 22° and 21° for device C and 34°, 29°, 31° and 31° for device D at wavelengths of 450 nm, 550 nm, 650 nm and 750 nm, respectively. Furthermore, the relative photocurrents of samples C and D alternates in intensity between angles at different incident light wavelengths. It is consistent with the observation of photoresponsivity curves in figure 4 and is attributed to the surface reflectivity and the defect related absorption described above.

The increase of the acceptance angle is mainly attributed to the nanopatterned surface as indicated from several reports [19–23] that surface morphology plays an important role in the wide incident angle of absorbance. For example, the effects of angle-independent reflectivity on anti-reflection surfaces have been discussed experimentally and theoretically [23, 24]. Moreover, we also notice larger acceptance angles of device D than those of device C at all the wavelengths measured. From the SEM photos in figure 3 along with the schematic plots in figure 1, device C shows a nanorod structure while device D possesses a nanocone morphology due to the coverage of both a-Si(i) and n-GZO layers. Typically, the nanocone structure has a wider incident angle of absorbance than the nanorod structure [21]. When the incident light is tilted, photons have more chance to fall within the angle of internal reflection for the nanocone structure and thus the acceptance angle is increased.

4. Conclusion

In this work, n-GZO/a-Si(i)/p^+-Si photodiodes are fabricated. As compared with the n-GZO/p^+-Si sample (device A), the photodiodes with nanopatterned a-Si(i) (device C) and nanopatterned p^+-Si substrate (device D) show 32% and 36.2% enhancement of photoresponsivity. And they also show main absorption peaks at the green wavelength range which is correlated to the a-Si(i) absorption. In comparison, the multi-absorption peaks for device A correspond to n-GZO, Si and

n-GZO/Si(i) junction absorptions. We also observe a blue shift of photoresponsivity spectra of nanopatterned devices as compared with that of a planar n-GZO/a-Si(i)/p^+-Si diode (device B), which is attributed to the more obvious decrease of reflectivity in the short wavelength range. Furthermore, the acceptance angle measurement reveals that the nanostructured photodiodes have larger acceptance angles than the planar one. For example, at 550 nm, the acceptance angle increases from 17° for device B to 25° and 29° for devices C and D, respectively. Our results also show that the nanocone structure of device D has a higher acceptance angle than the nanorod structure of device C. This work indicates that nanopatterned n-GZO/a-Si(i)/p^+-Si photodiodes have potential in solar cell applications.

Acknowledgment

This work was supported by the National Science Council of Taiwan under the grant 97-2221-E-002-054-MY3.

References

[1] Zhao J, Wang A, Green M A and Ferrazza F 1998 19.8% efficient 'honeycomb' textured multicrystalline and 24.4% monocrystalline silicon solar cells *Appl. Phys. Lett.* **73** 1991–3

[2] Zhao J, Wang A and Green M A 1999 24.5% efficiency silicon PERT cells on MCZ substrates and 24.7% effciency PERL cells on FZ substrates *Prog. Photovolt: Res. Appl.* **7** 471–4

[3] Campbell P and Green M A 1987 Light trapping properties of pyramidally textured surfaces *J. Appl. Phys.* **62** 243–9

[4] Gupta A and Compaan A D 2004 All-sputtered 14% CdS/CdTe thin-film solar cell with ZnO:Al transparent conducting oxide *Appl. Phys. Lett.* **85** 684–6

[5] Müller J, Rech B, Springer J and Vanecek M 2004 TCO and light trapping in silicon thin film solar cells *Sol. Energy* **77** 917–30

[6] Kluth O, Rech B, Houben L, Wieder S, Schope G, Beneking C, Wagner H, Loffl A and Schock H W 1999 Texture etched ZnO:Al coated glass substrates for silicon based thin flm solar cells *Thin Solid Films* **351** 247–53

[7] Tsakalakos L, Balch J, Fronheiser J, Korevaar B A, Sulima O and Rand J 2007 Silicon nanowire solar cells *Appl. Phys. Lett.* **91** 233117

[8] Stelzner T, Pietsch M, Andrä G, Falk F, Ose E and Christiansen S 2008 Silicon nanowire-based solar cells *Nanotechnology* **19** 295203

[9] Peters C H, Guichard A R, Hryciw A C, Brongersma M L and McGehee M D 2009 Energy transfer in nanowire solar cells with photon-harvesting shells *J. Appl. Phys.* **105** 124509

[10] Kim S K, Cho C H, Kim B H, Choi Y S, Park S J, Lee K and Im S 2009 The effect of localized surface plasmon on the photocurrent of silicon nanocrystal photodetectors *Appl. Phys. Lett.* **94** 183108

[11] Nakayama K, Tanabe K and Atwaterb H A 2008 Plasmonic nanoparticle enhanced light absorption in GaAs solar cells *Appl. Phys. Lett.* **93** 121904

[12] Pillai S, Catchpole K R, Trupke T and Green M A 2007 Surface plasmon enhanced silicon solar cells *J. Appl. Phys.* **101** 093105

[13] Takamoto T, Ikeda E, Kurita H and Ohmori M 1997 Over 30% efficient InGaP/GaAs tandem solar cells *Appl. Phys. Lett.* **70** 381–3

[14] Yang J, Banerjee A and Guha S 1997 Triple-junction amorphous silicon alloy solar cell with 14.6% initial and 13.0% stable conversion efficiencies *Appl. Phys. Lett.* **70** 2975–7

[15] Kim J Y, Lee K, Coates N E, Moses D, Nguyen T Q, Dante M and Heeger A J 2007 Efficient tandem polymer solar cells fabricated by all-solution processing *Science* **317** 222–5

[16] Chen C P, Lin P H, Chen L Y, Ke M Y, Cheng Y W and Huang J J 2009 Nanoparticle coated n-ZnO/p-Si photodiodes with improved photoresponsivities and acceptance angles for potential solar cell applications *Nanotechnology* **20** 245204

[17] Tanaka M, Taguchi M, Matsuyama T, Sawada T, Tsuda S, Nakano S, Hanafusa H and Kuwano Y 1992 Development of new a-Si/c-Si heterojunction solar cells: ACJ-HIT (artifically constructed junction heterojunction with intrinsic thin-layer) *Japan. J. Appl. Phys.* **31** 3518–22

[18] Tsuda S, Takahama T, Hishikawa Y, Tarui H, Nishiwaki H, Wakisaka K and Nakano S 1993 a-Si techologyies for high efficiency solar cells *J. Non-Cryst. Solids* **164–166** 679–84

[19] Huang Y F *et al* 2007 Improved broadband and quasiomnidirectional anti-reflection properties with biomimetic silicon nanostructures *Nat. Nanotechnol.* **2** 770–4

[20] Yang Z P, Ci L, Bur J A, Lin S Y and Ajayan P M 2008 Experimental observation of an extremely dark material made by a low-density nanotube array *Nano Lett.* **8** 446–51

[21] Zhu J, Yu Z, Burkhard G F, Hsu H M, Connor S T, Xu Y, Wang Q, MeGehee M, Fan S and Cui Y 2009 Optical absorption enhancement in amorphous silicon nanowire and nanocone arrays *Nano Lett.* **9** 279–82

[22] Min W L, Jiang B and Jiang P 2008 Bioinspired self-cleaning antireflection coatings *Adv. Mater.* **20** 3914–8

[23] Li Y *et al* 2009 Biomimetic surfaces for high-performance optics *Adv. Mater.* **21** 4731–4

[24] Dobrowolski J A, Poitras D, Ma P, Vakil H and Acree M 2002 Toward perfect antireflection coatings: numerical investigation *Appl. Opt.* **41** 3075–83